# Rayleigh-Bénard convection in 3He near its critical point

Madiha Bouafia, Olivier Daube

# Rayleigh-Bénard convection in $^3He$ near its critical point

Madiha Bouafia[a,*], Olivier Daube[a]

[a]*LMEE, Univ. Evry, Université Paris-Saclay, 91020, Evry, France*

**Abstract**

We study by direct numerical simulation the Rayleigh-Bénard convection in supercritical $^3He$ using an anelastic approximation. The latter is based on scaling analysis associated with asymptotic expansions of the full governing equations which has an important consequence for numerical integration of the model. The approximate equations are supplemented by a parametric state equation and are solved numerically by a finite difference method coupled with a projection method. Numerical results giving time evolutions of the temperature difference between the horizontal walls are calculated and compared to experimental data. The convection onset is examined for the studied configuration.

*Keywords:* Anelastic approximation, Rayleigh-Bénard convection, supercritical fluid, transient flow, piston effect.

*Corresponding author : Madiha Bouafia, bouafia@univ-evry.fr

**Nomenclature**

| | |
|---|---|
| $A$ | aspect ratio, $A = L/H$ |
| $ATG$ | adiabatic temperature gradient |
| $c_p$, $c_v$ | specific heat capacities |
| $H$ | height |
| $L$ | width |
| $E_k$ | reduced total kinetic energy |
| $Eu$ | Euler number |
| $F$ | Froude number |
| $G_h$ | dimensionless number |
| $\overline{P}$ | mean thermodynamic pressure |
| $P_s$ | hydrostatic pressure |
| $Pr$ | Prandtl number |
| $q$ | heat flux density ($Wm^{-2}$) |
| $Re$ | Reynolds number |
| $Ra$ | Raleigh number |
| $Ra_{mod}$ | modified Rayleigh number |
| $T_i$ | initial temperature |
| $t_0$ | time scale |
| $t_D$ | diffusion time |
| $t_{ep}$ | time of the piston effect |

| *Greek symbols* | |
|---|---|
| $\beta$ | isobaric thermal expansion, $K^{-1}$ |
| $\gamma$ | ratio of specific heats |
| $\Delta T$ | Temperature difference between the horizontal walls, $\mu K$ |
| $\varepsilon$ | reduced temperature parameter, $\varepsilon = \frac{T_i - T_c}{T_c}$ |
| $\theta$ | scale of the temperature difference, $\theta = \frac{qH}{T_c k}$ |
| $\kappa$ | thermal conductivity, $W^{-1}K^{-1}$ |
| $\mu$ | dynamic viscosity, $kgm^{-1}s^{-1}$ |
| $\rho$ | density |
| $\rho_s$ | density stratification |

| *Subscripts* | |
|---|---|
| 0 | reference value |
| $b$ | bottom |
| $c$ | value at critical point |

## 1. Introduction

Transport properties of pure fluids display large variations when approaching the gas-liquid critical point. In such fluids, the thermal diffusivity tends to zero

while the isothermal compressibility, the thermal expansion coefficient and the isobaric specific heat diverge. These behaviors lead to a specific mechanism of heat transfer called the piston effect (PE) which induces a rapid homogenization of the temperature by thermoacoustic effects. The PE was initially observed experimentally in micro-gravity by [1] then evidenced theoretically by [2]-[4].
The interest shown the last two decades on the hydrodynamic stability of supercritical fluids is reflected in a significant number of experimental [5]-[6], theoretical [7]-[8] and numerical works [9]-[11]. One of the configurations that quickly emerged as a study model is the Rayleigh-Bénard convection because of the interaction between two stability criteria: the classical Rayleigh criterion valid in Boussinesq and the Schwarzschild criterion valid for atmospheric flows at large scales. In supercritical fluids, the Schwarzchild criterion becomes relevant on small scales of length, including cells with very small dimensions due to the divergence of the compressibility [12]-[13]. A modified Rayleigh number was proposed by [14] including the difference between the real gradient and the adiabatic temperature gradient. The latter, $ATG = \rho g(\partial T/\partial P)_s$, is related to an adiabatic process and corresponds to the temperature gradient obtained by moving a fluid particle along the hydrostatic pressure gradient. It has a stabilizing effect in the convection onset and its role is becoming increasingly important when approaching the critical point [5].

The primary goal of this paper is to validate the use of the anelastic approximation for supercritical fluids. The paper basically consists of two parts. The first one is devoted to describe the set of approximations applied to full compressible Navier-Stokes equations based on an anelastic approximation. Another important point of our work lies in the use of a parametric state equation of supercritical $^3He$. It has the advantage to reproduce accurately physical properties of the fluid near the critical point. The anelastc equations allow to simulate the Rayleigh-Benard convection in supercritical fluids driven by a weak heating from below. A method is proposed to solve the derived equations. The second part is devoted to 2D numerical results obtained in the same conditions as in experiments described in [6]. The validation of the code is done by comparing numerical solutions to experimental data. The convection onset is also examined through the influence of the aspect ratio on the total kinetic energy, and temperature fields during the transient phase.

## 2. CONFIGURATION

Following the experimental studies [6], we are interested in the onset of the Rayleigh-Bénard convection in the supercritical $^3He$, for modified Rayleigh numbers above the instability threshold. A thin layer of $^3He$ ($H = 1.06mm$) is bounded by two horizontal plates. The fluid is initially at rest with conditions

close to the critical point $(\rho_c, p_c, T_c)$= $(41.45kg/m^3, 1.1510^5Pa, 3.31K)$.

- The initial temperature in the cavity is uniform and slightly greater than $T_c$. The distance to the critical point is characterized by $\epsilon = \frac{(T_i - T_c)}{T_c}$.
- The fluid is initially stratified with an mean value equal to the critical density $\rho_c$.

The bottom wall is heated with a uniform heat flux while the upper one is maintained at the initial temperature $T_i$ (fig.1). The considered values of the heat flux $q$ are such as $(T - T_i)/(T_i - T_c)$ is always « 1. This allowed us to consider that the dynamic viscosity $\mu$, the thermal conductivity $k$, the specific heat $c_p$ and the coefficient of the isobaric thermal expansion $\beta$ remain constant in the considered temperature interval with values taken at the initial temperature $T_i$.

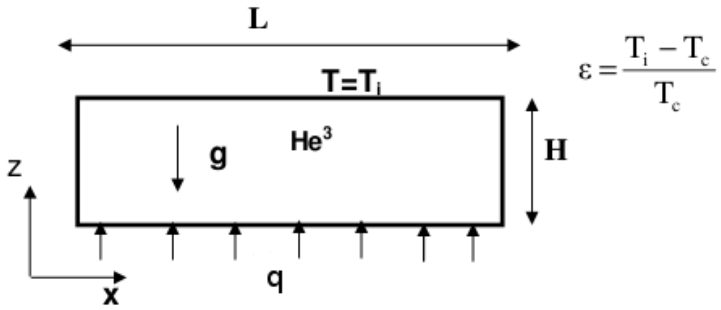


Figure 1: Supercritial $^3He$ in Rayleigh-Benard configuration.

## 3. GOVERNING EQUATIONS

The values of the heat flux $q$ and the parameter $\epsilon$ considered in this study allow us to assume that:

- the physics of the phenomena considered in this work may be described in the framework of continuum mechanics. The flow is therefore governed by the full compressible Navier-Stokes equations. We have chosen to use the enthalpy form of the energy equation and the equation of state in a parametric form fitted to experimental data [15].
- the dynamic viscosity $\mu$, the thermal conductivity $k$, the specific heat $c_p$ and the isobaric thermal expansion coefficient $\beta$ remain constant in the considered temperature interval and equal to their values at the initial temperature $T_i$.

Using the following reference quantities (the subscript $_c$ refers to values at the critical point):

- length: $L_0 = H$, the fluid layer thickness;
- Pressure: $P_0 = p_c$; Density: $\rho_0 = \rho_c$; Temperature: $T_0 = T_c$
- Velocity: $V_0$ = a characteristic velocity of the flow which tends to zero when the heating flux $q$ responsible for the flow tends to zero.
- Time: $t_0 = L_0/V_0$

the governing equations in dimensionless form read:

$$\begin{aligned}
\frac{\partial \rho}{\partial t} + \nabla \cdot (\rho \overrightarrow{\mathbf{V}}) &= 0 \\
\rho \frac{\mathrm{d}\overrightarrow{\mathbf{V}}}{\mathrm{dt}} &= -Eu \nabla p + \frac{1}{\mathrm{Re}} \nabla \cdot \overline{\overline{\tau}} - \frac{1}{\mathrm{F}^2} \rho \overrightarrow{\mathbf{z}} \\
\rho \frac{\mathrm{d}T}{\mathrm{dt}} &= \frac{1}{\mathrm{PrRe}} \nabla^2 T + G_h \beta(T_i) T_i \frac{\mathrm{d}p}{\mathrm{dt}} \\
p &= f(\rho, T)
\end{aligned}$$

where $\beta = -\frac{1}{\rho}\left(\frac{\partial \rho}{\partial T}\right)_p$ is the isobaric thermal expansion coefficient and the stress tensor $\overline{\overline{\tau}}$ is defined by: $\overline{\overline{\tau}} = \frac{1}{2}\left(\nabla \overrightarrow{\mathbf{V}} + \nabla \overrightarrow{\mathbf{V}}^t\right) + \frac{\nabla \cdot \overrightarrow{\mathbf{V}}}{3} \overline{\overline{\mathbf{I}}}$

with the following dimensionless parameters:

$\mathrm{Re} = \dfrac{\rho_c V_0 H}{\mu}$ Reynolds number $\quad \mathrm{Eu} = \dfrac{p_c}{\rho_c V_0^2}$ Euler number $\quad G_h = \dfrac{p_c}{\rho_c c_p T_c}$

$\mathrm{Pr} = \dfrac{\mu c_p}{k}$ Prandtl number $\quad \mathrm{F} = \dfrac{V_0}{\sqrt{gH}}$ Froude number $\quad \gamma = \dfrac{c_p}{c_v}$ ratio of specific heats

## 4. THE ANELASTIC APPROXIMATION

In the context of a numerical simulation, the main difficulties arise from the fact that the compressible Navier-Stokes equations support acoustic waves. Though these waves are not important in this Rayleigh-Bénard configuration as they do not contribute in a significant way to energy transfer compared to convective effects, they involve very restrictive stability criteria for the numerical simulation. In order to overcome these drawbacks, they are filtered out by using a so-called low Mach number approximation (LMNA), taking advantage of the low speed nature of the convective effects. More precisely, a particular kind of LMNA is used, namely anelastic approximation used for instance in stratified geophysical flows.

For this purpose, an analysis of the orders of magnitude of the different terms shows that $Eu \gg 1$. A regular asymptotic expansion is then performed by expanding all the primary variables in powers of the small parameter $\eta = 1/Eu$:

$$\begin{aligned} p &= p^{(0)} + \eta p^{(1)} + O(\eta^2) \\ \rho &= \rho^{(0)} + \eta \rho^{(1)} + O(\eta^2) \\ \overrightarrow{\mathbf{V}} &= \overrightarrow{\mathbf{V}}^{(0)} + \eta \overrightarrow{\mathbf{V}}^{(1)} + O(\eta^2) \\ T &= T^{(0)} + \eta T^{(1)} + O(\eta^2) \end{aligned}$$

Inserting these expansions into the Navier-Stokes equations, a sequence of an $O(\eta^{-1})$ and of an $O(1)$ problems is obtained:

*4.1. $O(\eta^{-1})$ order problem*

$$\nabla p^{(0)} + \frac{1}{\mathrm{Eu\,F^2}} \rho^{(0)} + \frac{1}{\mathrm{Eu\,Re}} \nabla \cdot \overline{\overline{\tau}}^{(0)} = 0 \qquad (1)$$

where

$$\frac{1}{\mathrm{Eu\,F^2}} = \frac{\rho_c g H}{p_c} \quad \text{and} \quad \frac{1}{\mathrm{Eu\,Re}} = \frac{\mu V_0}{p_c H}$$

The first term of (1) is a pure $O(\eta^{-1})$ order term and will thus be kept. The second and third terms of (1) behave differently when $q$ increases:

- In the framework of continuum mechanics the Knudsen number is $\ll 1$. Thus, the kinetic gas theory involves that the parameter $\dfrac{1}{\mathrm{Eu\,Re}}$ is $\ll 1$ .
- The parameter $\dfrac{1}{\mathrm{Eu\,F^2}}$ is small but its value is fixed since it does not depend on the distance to the critical point nor on the input heat flux,

Therefore, only the two first terms of (1) are retained in the zero$^{th}$ problem yielding:

$$\nabla p^{(0)} + \frac{1}{\mathrm{Eu\,F^2}} \rho^{(0)} \overrightarrow{\mathbf{z}} = 0$$

This equation involves that $p^{(0)}$ and the density $\rho^{(0)}$ do not depend on $x$ nor $y$. The pressure therefore may be split into two parts:

$$p^{(0)}(z,t) = \overline{P}(t) + p_s(z)$$

where $\overline{P}(t) = \int_0^1 p^{(0)}(z,t)\,dz$ is the average thermodynamic pressure and $(p_s(z), \rho_s(z) = \rho^{(0)}(z))$ are the initial pressure and density stratification, solutions of the system:

$$\frac{dp_s}{dz} + \frac{1}{\mathrm{Eu\,F^2}}\rho_s(z) = 0 \tag{2}$$

$$p_s = f(\rho_s, T_i) \tag{3}$$

subject to the constraints:

$$\int_0^1 \rho_s(z)\,dz = 1 \tag{4}$$

$$\int_0^1 p_s(z)\,dz = 0 \tag{5}$$

*4.2. Zero$^{(th)}$ order problem*

Once the $\eta^{-1}$ order problem is solved, the zero$^{(th)}$ order problem reads:

$$\begin{aligned}
\frac{\partial \rho^{(0)}}{\partial t} + \nabla \cdot (\rho^{(0)} \overrightarrow{\mathbf{V}}^{(0)}) &= 0 \\
\rho^{(0)} \frac{\mathrm{d}\overrightarrow{\mathbf{V}}^{(0)}}{\mathrm{dt}} &= -\nabla p^{(1)} + \frac{1}{\mathrm{Re}} \nabla \cdot \overline{\overline{\tau}}^{(0)} - \frac{1}{\mathrm{EuF^2}} \rho^{(1)} \overrightarrow{\mathbf{z}} \\
\rho^{(0)} \frac{\mathrm{d}T^{(0)}}{\mathrm{dt}} &= \frac{1}{\mathrm{PrRe}} \nabla^2 T^{(0)} + G_h (\beta T)_{T_i} \left( \frac{\mathrm{d}\overline{P}}{\mathrm{dt}} + \overrightarrow{\mathbf{V}}^{(0)} \cdot \nabla p^{(0)} \right) \\
p^{(0)}(z) &= f(\rho^{(0)}, T^{(0)})
\end{aligned}$$

Replacing $\rho^{(1)}$ by its first order approximation $(\rho - \rho^{(0)})/\eta$ and taking into the fact that $\dfrac{1}{\mathrm{Eu\,F^2}}$ is finite and that $\rho^{(0)} = \rho_s$ is independent of the time $t$, the first order problem finally reads:

$$\nabla \cdot (\rho_s \overrightarrow{\mathbf{V}}) = 0 \qquad \text{continuity equation} \tag{6}$$

$$\rho_s \frac{\mathrm{d}\overrightarrow{\mathbf{V}}}{\mathrm{dt}} = -\nabla\pi + \frac{1}{\mathrm{Re}}\nabla \cdot \overline{\overline{\tau}} - \frac{1}{\mathrm{F}^2}(\rho - \rho_s)\overrightarrow{\mathbf{z}} \qquad \text{momentum equation} \tag{7}$$

$$\rho_s \frac{\mathrm{d}T}{\mathrm{dt}} = \frac{1}{\mathrm{PrRe}}\nabla^2 T + G_h(\beta T)_{T_i}\left(\frac{\mathrm{d}\overline{P}}{\mathrm{dt}} + \overrightarrow{\mathbf{V}} \cdot \nabla p_s\right) \qquad \text{energy equation} \tag{8}$$

$$\overline{P}(t) + p_s(z) = f(\rho, T) \qquad \text{equation of state} \tag{9}$$

$$\int_V \rho d\upsilon = L/H \qquad \text{global mass conservation} \tag{10}$$

Where the superscripts $^{(0)}$ and $^{(1)}$ have been dropped and $\pi$ stands for $p^{(1)}$. We can notice that this model derived from an anelastic approximation, differs slightly from the one proposed by Accary *et al* [10], in particular with the use of $\rho_s$ instead of $\rho$ everywhere excepted in the buoyancy term. Our model may thus be seen as an extended Boussinesq approximation using a stratified density field instead of a uniform one.

## 5. BOUNDARY CONDITIONS

The classical no-slip condition $\overrightarrow{\mathbf{V}} = 0$ on the walls is used for the velocity. Concerning the temperature, different sets of boundary conditions were used on the horizontal walls whereas the side boundaries are adiabatic:

1. Dirichlet: in this case, the horizontal lower plate is maintained at an uniform temperature $T_b(t)$,
2. In experimental data, the heating is performed using a uniform heat flux $q(W/m^2)$. Two kind of boundary conditions were used in the numerical simulations to ensure the proper heat flux.
   (a) The given heat flux $q(t)$ is imposed pointwise by means of a Neumann condition,
   (b) Due to the huge discrepancy between the thermal conductivities of the fluid and of the copper plates used in the experiments, we assumed that the temperature $T_b$ of the bottom plate is uniform in space and depends only on the time $t$, i.e. $T_b = T_b(t)$. An additional

constraint has therefore to be imposed to ensure the correct overall heat flux, namely:

$$-k\frac{1}{A}\int_0^A \left.\frac{\partial T}{\partial z}\right|_{z=0} dx = q(t) \tag{11}$$

## 6. NUMERICAL METHODOLOGY

Centered mimetic finite differences on a staggered MAC mesh are used for the spatial discretization [16]. The grid is uniform in the x-direction and variable in z. The time derivatives are approximated by a second order backward Euler scheme in which the linear terms are treated implicitly while the non linear terms are treated explicitly with an Adams-Bashforth extrapolation. Giving the solution $(\overrightarrow{\mathbf{V}}^{(n)}, p^{(n)}, T^{(n)}, \rho^{(n)})$ at time level $n\Delta t$, it is well known (see for instance [17]) that the solution at time level $(n+1)\Delta t$ may be obtained by solving the following sequence of problems:

1. *Resolution of the energy equation*

$$\left(\rho_s\sigma_T \mathrm{I} - \nabla^2\right)T^{n+1} = S_T^{n,n-1} + G_h\left[\beta T\right]_{T=T_i}\left(\frac{\mathrm{d}\overline{P}^{n+1}}{\mathrm{dt}} + \overrightarrow{\mathbf{V}}^n \cdot \nabla p_s\right) \tag{12}$$

2. *Computation of* $\rho^{(n+1)}$, $\overline{P}^{(n+1)}$: the following system of nonlinear equations consisting of the equation of state written at each point of the mesh and of an additional condition imposing the conservation of total mass is solved by Newton-Raphston's method:

$$\overline{P}^{n+1}(t) + p_s(z) = f(\rho^{n+1}, T^{n+1}) \tag{13}$$

$$\int_V \rho^{n+1} d\upsilon = L/H \tag{14}$$

3. *Computation of* $\dfrac{\mathrm{d}\overline{P}^{n+1}}{\mathrm{dt}}$ : along the lines of [18] , a compatibility condition for $\dfrac{\mathrm{d}\overline{P}^{n+1}}{\mathrm{dt}}$ is obtained by integrating on the whole domain $\Omega$ the energy equation and taking into account the continuity equation:

$$\frac{\mathrm{d}\overline{P}^{n+1}}{\mathrm{dt}} = \frac{1}{A}\int_{\partial\Omega} \frac{\partial T}{\partial \overrightarrow{\mathbf{n}}}\, dl \tag{15}$$

4. *Resolution of the momentum and continuity equations*

$$\nabla \cdot (\rho_s \overrightarrow{\mathbf{V}}^{n+1}) = 0 \tag{16}$$

$$\left(\rho_s\sigma_V \mathrm{I} - \boldsymbol{\nabla}^{\,2}\right)\overrightarrow{\mathbf{V}}^{n+1} + \mathrm{Re}\nabla\pi^{n+1} = \overrightarrow{\mathbf{S}}_V^{n,n-1} - \frac{\mathrm{Re}}{\mathrm{F}^2}(\rho^{n+1} - \rho_s)\overrightarrow{\mathbf{z}} \tag{17}$$

where $\sigma_V = 3\mathrm{Re}/2\Delta t$ and $\sigma_T = 3\mathrm{PrRe}/2\Delta t$. The source terms are respectively given by:

$$S_T^{n,n-1} = \mathrm{PrRe}\left(\rho_s \frac{4T^n - T^{n-1}}{2\Delta t} - 2(\rho_s \overrightarrow{\mathbf{V}} \cdot \nabla T)^n + (\rho_s \overrightarrow{\mathbf{V}} \cdot \nabla T)^{n-1}\right)$$

$$\overrightarrow{\mathbf{S}}_V^{n,n-1} = \mathrm{Re}\left(\rho_s \frac{4\overrightarrow{\mathbf{V}}^n - \overrightarrow{\mathbf{V}}^{n-1}}{2\Delta t} - 2(\rho_s \overrightarrow{\mathbf{V}} \cdot \nabla \overrightarrow{\mathbf{V}})^n + (\rho_s \overrightarrow{\mathbf{V}} \cdot \nabla \overrightarrow{\mathbf{V}})^{n-1}\right)$$

The coupling $\overrightarrow{\mathbf{V}}$–$\pi$ is treated by a classical projection method for incompressible flows [19] applied to $\rho_s \overrightarrow{\mathbf{V}}$. The resolution is split in two steps:

- *prediction*: $\rho_s \overrightarrow{\mathbf{V}}^{(n)} \longrightarrow \rho_s \overrightarrow{\mathbf{V}}^{(*)}$

  $$\left(\rho_s \sigma_V \mathrm{I} - \boldsymbol{\nabla}^{\,2}\right)\overrightarrow{\mathbf{V}}^* + \mathrm{Re}\nabla\pi^n = \overrightarrow{\mathbf{S}}_V^{n,n-1} - \frac{\mathrm{Re}}{\mathrm{F}^2}(\rho^{n+1} - \rho_s)\overrightarrow{\mathbf{z}}$$

  supplemented by the no–slip condition $\overrightarrow{\mathbf{V}}^* = 0$ on the boundaries.

- *correction*:
  $\rho_s \overrightarrow{\mathbf{V}}^{(n+1)} = \rho_s \overrightarrow{\mathbf{V}}^{(*)} + \nabla\varphi$, where $\varphi$ is calculated in order to satisfy $\nabla \cdot (\rho_s \overrightarrow{\mathbf{V}}^{(n+1)}) = 0$

In order to ensure at each time step the correct heat flux (11), the following procedure holds: In a preprocessing step, a particular problem is solved:

$$\left(\rho_s \sigma_T \mathrm{I} - \nabla^2\right)\widehat{T} = 0 \text{ in } \Omega \tag{18}$$

$$\frac{\partial \widehat{T}}{\partial x}(0, z) = \frac{\partial \widehat{T}}{\partial x}(A, z) = 0 \tag{19}$$

$$\widehat{T}(x, 0) = 1 \tag{20}$$

$$\widehat{T}(x, 1) = 0 \tag{21}$$

and its solution $\widehat{T}$ is stored. During the time marching process described in section 6, the energy equation (12) is solved with an arbitrary value $\widetilde{T}_b$ of the temperature along the bottom plate, yielding a provisional field $\widetilde{T}$. The actual temperature filed $T$ reads then

$$T = \widetilde{T} + \lambda \widehat{T}$$

where $\lambda$ is computed in order to satisfy the flux condition (11).

## 7. STATE EQUATION

A parametric state equation defined in [15] is used to describe the $(P, \rho, T)$ dependence for supercritical $^3He$. This equation includes a regular part which matches the properties of the fluid far away of the critical point and a singular part containing the universality of the fluid behavior close to the critical point, especially the critical exponents.

## 8. VALIDATION

The results reported in this section are performed on a horizontal cell of aspect ratio $A = L/H = 4$. A grid points $769 \times 129$ is used on a uniform mesh in the x direction and on a non-uniform hyperbolic tangent mesh in the z direction.

### *8.1. Criterion for convection onset*

The code has been tested first by finding the Rayleigh-Schwarzschild criterion of the convection onset. According to [14], the threshold of the instability onset is given by the modified Rayleigh number:

$$Ra_{mod} = \frac{\rho_c^2 c_p g \beta H^4}{k\mu} \left( \frac{\Delta T}{H} - g \frac{T_i \beta}{c_p} \right) \geq Ra_c$$

Where $\frac{\Delta T}{H}$ is the temperature gradient between the horizontal walls and $g\frac{T_i\beta}{c_p}$ the adiabatic temperature gradient ATG. For a distance to the critical point $\epsilon = 0.02$, ATG is equal to 0.034 mK/cm. The critical Rayleigh number $Ra_c$ which depends on the boundary layers is equal to 1708 for a configuration with two solid walls [20]. The critical temperature difference between the horizontal walls at which the convection starts is then given by: $\Delta T_{onset} = ATG \times H + Ra_c(k\mu/\rho_c^2 c_p g \beta H^3)$. In order to determine the stability threshold, we plot the total reduced kinetic energy $E_c$ as a function of the modified Rayleigh number when the bottom wall is maintained at a uniform temperature or subjected to a uniform heat flux. The total kinetic energy is equal to $E_k = \frac{1}{2}\int_0^1 \int_0^A \rho V^2 dx dz$. Figure 2 shows the variations of $E_k$ versus the modified Rayleigh number. With a uniform temperature, the transition to a convective motion occurs at a critical value $Ra_c \simeq 1811$ and the corresponding temperature difference $\Delta T$ between the horizontal walls is equal to 0.041 mK. In the case of a uniform heat flux, the transition is located close to $Ra_c \simeq 1743$ for the range $7.4 \times 10^{-5} < q < 7.5 \times 10^{-5} \quad W/m^2$.

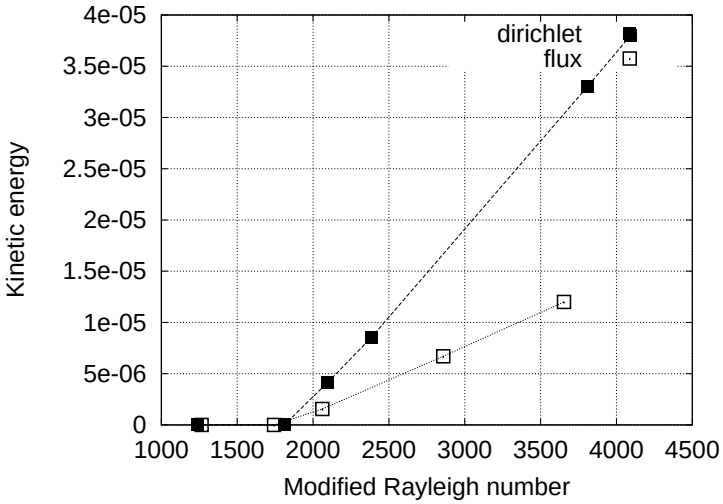


Figure 2: Total kinetic energy versus the modified Rayleigh number.

*8.2. Impact of the piston effect*

When the heating starts, the fluid temperature inside the cavity increases rapidly due to the piston effect. Owing to the high compressibility and the very small diffusivity, the heating from below induces the appearance of three distinct zones : two thermal boundary layers near the top and bottom walls in which heat transfer is done by diffusion and the bulk of cavity which heated up adiabatically and homogeneously. The presence of the piston effect modifies the temperature field compared with an ordinary process of diffusion. Figure 3 shows profiles of the reduced temperature $(T - T_{z=H})/\theta$ at different instants, where $\theta = \frac{qH}{T_c k}$ is a scale of the temperature difference. In the diffusion regime, typical profiles of temperatures are characterized by a rapid and homogeneous temperature in the bulk region during action of the piston effect. The characteristic time of the piston effect is $t_{ep} = 0.18s$ while the diffusion time $t_D = 5.4 \times 10^2 s$. The piston effect is equal to $t_{ep} = \frac{t_D}{(\gamma-1)^2}$ [2], and the diffusion characteristic time is equal $T_D = \frac{H^2}{k/\rho_c c_p}$ where $k/\rho_c c_p$ denotes the thermal diffusivity at critical density for the ideal gas.

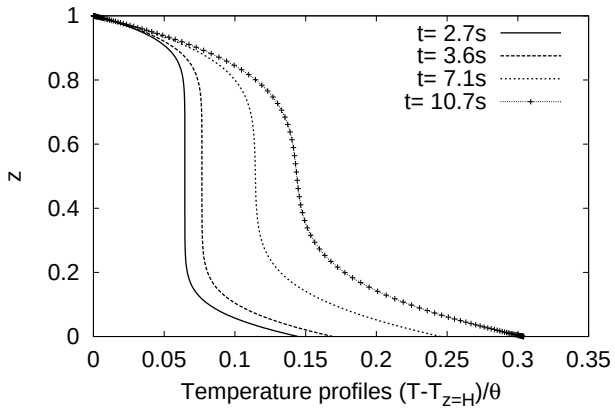


Figure 3: Vertical profiles of temperature at $x = 0.5$ for $q = 1.69 \times 10^{-3} W/m^2$ and $\epsilon = 0.02$.

## 9. NUMERICAL SIMULATIONS

In this section, we are interested in fluid heated from below with a uniform heating $q = 1.69 \times 10^{-3} W/m^2$ and for a distance to the critical point $\epsilon = 0.02$. This configuration allows comparison between our numerical results and experiments available in the literature [6]. The simulations are based on thermophysical properties : $c_p = 2.19 \times 10^5 J/kg/K$, $k = 1.89 \times 10^{-2} W/m/K$; $\mu = 1.83 \times 10^{-6} m^2/s$ and $\beta = -\frac{1}{\rho}\frac{\partial \rho}{\partial T} = 22.1 K^{-1}$. The other dimensionless parameters are : $Re = 139$, $Pr = 21.2$, $Eu = 8 \times 10^7$, $F = 3 \times 10^2$ and $\gamma = 55.4$. The time step $\Delta t$ is equal to 1/10 of the characteristic time of the piston effect $t_{ep}$. The values of time scales are $0.18s$ and $540s$ for $t_{ep}$ and $T_D$ respectively.

### *9.1. Comparison with experimental data*

Figure 4 displays time evolutions of the temperature difference $\Delta T(t)$ obtained from computations and experimental data of reference [6]. The simulations were carried out with different state equations of $^3He$ near its critical point : the parametric law according to [15] and analytic laws (Van der Walls, Redlich Kwong). One can observe that the profiles related to analytic laws are identical. All the relaxation curves show similar behavior : an initial phase with a quasi-linear evolution until attaining a maximum (first peak since the heating starts) followed by a second phase characterized by damped oscillations before reaching a quasi-steady state. These oscillations have also been observed experimentally and are attributed to the interaction between the diffusion and piston effect [21]. Note that the curve relating to the parametric law shows better agreement with the experimental results, in particular the period of

pseudo oscillations and the quasi-steady value of $\Delta T(t)$. On the other hand, the return "from below" to the asymptotic state observed experimentally is not found in the calculations as in all published numerical simulations. Note finally that the relaxation curves strongly depend on the heating flux $q$ and the proximity to the critical point $\epsilon$ as shown in experiments of Kogan and Meyer [5],[12].
To examine the impact of aspect ratio on the $\Delta T(t)$ profiles, simulations were carried out with three values $A = 4, 8$ and 16. We point out that the experiments were conducted in a shallow cavity with aspect ratio equal to 57. The numerical results displayed in figure 5 reveal once again deviations between experiment and simulations during the transient phase. The high of the first peak remains larger in simulations and does not vary with the aspect ratio. For $A = 16$, the amplitudes of damped oscillations are lower than for $A = 4$ or $A = 8$ but the locations of extrema are not well synchronized with experimental data.

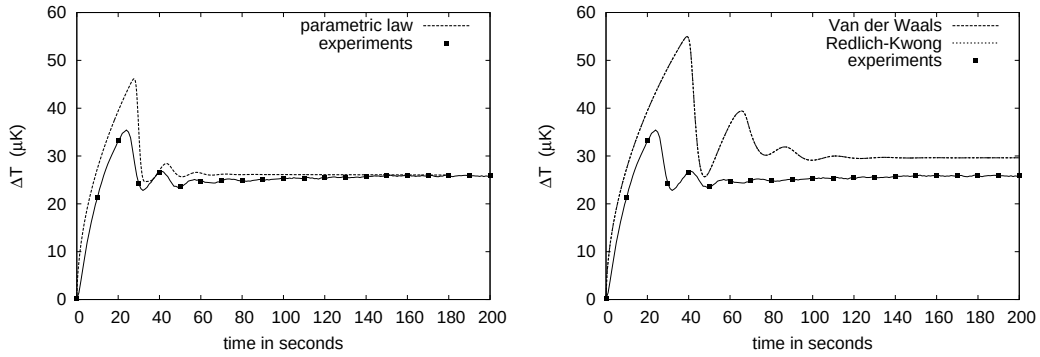


Figure 4: Experimental and numerical profiles $\Delta T(t)$ from $2D$ computations for $q = 1.69 \times 10^{-3} W/m^2$, $\epsilon = 0.02$ and aspect ratio $A = 2$.

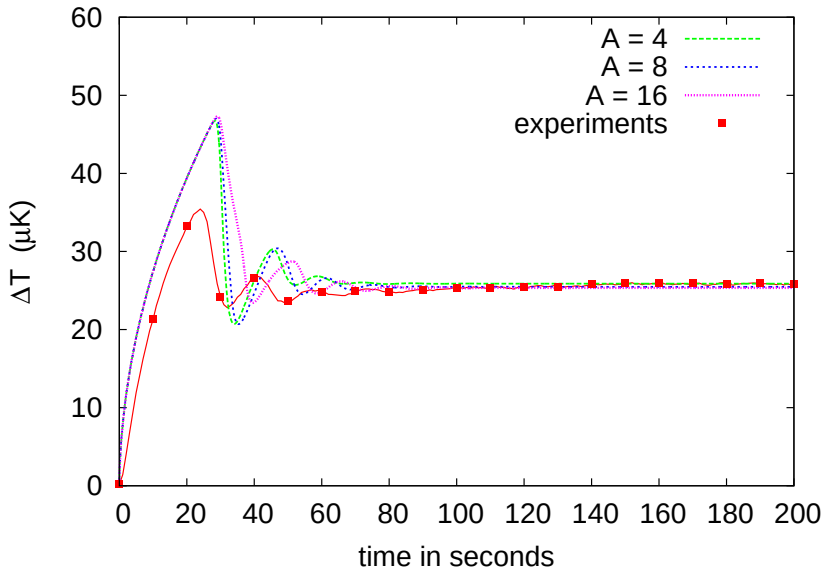


Figure 5: Comparison between experimental and numerical profiles of $\Delta T(t)$ for $q = 1.69 \times 10^{-3} W/m^2$ at $\epsilon = 0.02$ and aspect ratios $A = 4, 8, 16$.

### *9.2. Convection onset*

We examine first the influence of aspect ratio on the convection onset. Figure 6 shows transient profiles of $\Delta T$ and total kinetic energy as function of time for three values ($A = 4, 8, 16$) on a short period up to $40s$. The figure shows principally two phases: a first one where the kinetic energy is insignificant, followed by a second one where the kinetic energy increases rapidly and attains a maximum which coincides with the maximum of $\Delta T$ profile. As can be seen, the convection is triggered at the same time whatever the aspect ratio before the profiles merge during the ascent phase. Snapshots of the kinetic energy are displayed in figure 7 at $t \simeq 17s$ to evidence this point. Only the left half of each cavity is represented since the profiles of kinetic energy are symmetric. One can see that the convective starts first at the edges in the same proportions regardless the aspect ratio.
Figure 8 shows snapshots of temperature fields at different instants for a cavity with aspect ratio $A = 8$. The corresponding times are marked on figure 9 to locate them on the $\Delta T$ profile. During the initial phase, figures 8(A,B) exhibits temperature fields still dominated by the diffusive regime although weak irregularities appear on the isotherms of fig.8(B). Figure 8(C) shows the development of thermal plumes at the extremities then gradually cover the whole space between the horizontal walls as $\Delta T$ increases. On figure 6, the first peak of kinetic energy located at $t \simeq 30s$ indicates that convection has developed substantially which nearly coincides with the maximum of $\Delta T(t)$.

at time $t = 32s$ , figure 8 (D) shows that a cooling is initiated as a result of the fluid movement from the cold top region to the bottom. When approaching the second pick (minimum), an excess cooling leads to an homogeneous temperature in the bulk which is the signature of the piston effect (fig.8(E) at $t \simeq 36s$). Figures 8(F,G) give the temperature profiles corresponding to moments approaching the quasi-steady state. Isotherms display upward and downward thermal plumes arising from the horizontal walls.
The role of the piston effect (PE) on the damped oscillations has been described and argued by Amiroudine and Zappoli in [21]. According to their description, when the bulk temperature increases sufficiently (thermal plumes cover the whole space after the heating starts), the temperature gradient at the cold top boundary increases. The cold piston effect is then operative driving the cold fluid downwards. It leads to a decrease of the temperature and to the first peak in the $\Delta T$ profile. An excess cooling of the bulk increases the temperature gradient at the bottom boundary. The hot piston effect becomes then dominant driving the hot fluid upwards, thus producing a minimum in $\Delta T$, and so on.

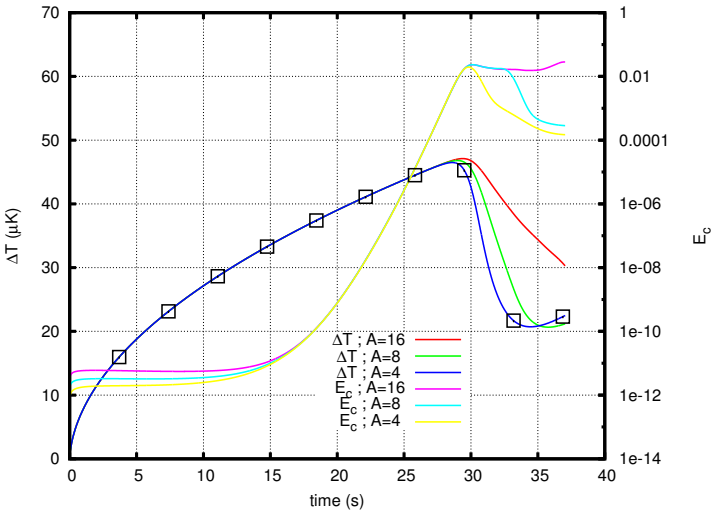


Figure 6: Time evolution of the kinetic energy $E_c$ and $\Delta T$ for $A = 4, 8, 16$.


Figure 7: Snapshot of Kinetic energy for $A = 4, 8, 16$ at time $t \simeq 17s$.

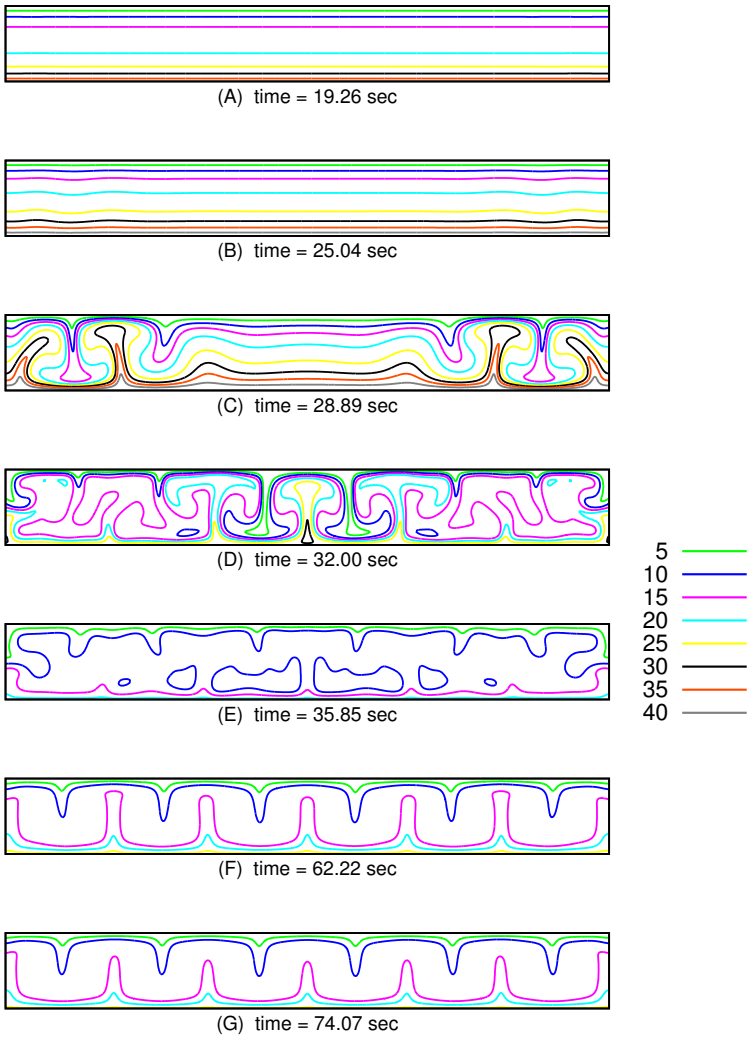


Figure 8: Temperature fields at different instants : $q = 1.69 \times 10^{-3} W/m^2$, $\epsilon = 0.02$ and $A = 8$.

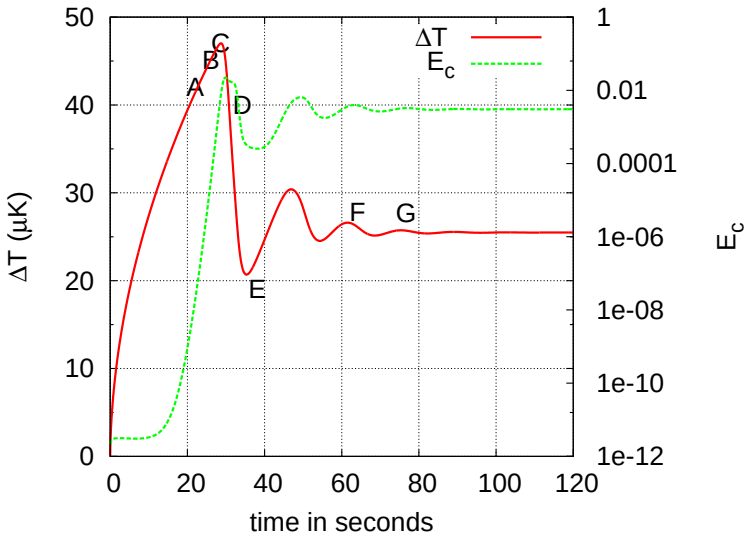


Figure 9: Time Evolution of the temperature difference $\Delta T$ and the reduced kinetic energy $E_c$ for $q = 1.69 \times 10^{-3} W/m^2$, $\epsilon = 0.02$ and $A = 8$.

## 10. Conclusion

We presented a hydrodynamic model to study Rayleigh-Bénard convection in supercritical fluids within an anelastic approximation. The model is then applied to two-dimensional numerical simulations of a thin layer of supercritical $^3He$ heated from below, in the same conditions as in experiments mentioned in [6]. A parametric state equation is used which has the advantage to reproduce accurately physical properties of the fluid near the critical point. The main results in this study are summarized as follows:

- Rayleigh-Schwarzchild instability criterion for the convection onset has been highlighted in the presence of the piston effect.
- Numerical profile of $\Delta T(t)$ exhibits deviations with experimental curve during the initial phase but agree well at quasi-steady state. The use of a parametric state equation gives better results than do analytic laws.
- Convection onset does not change with the the aspect ratio.

**Acknowledgements**
We are grateful to Pierre Carlès for his contribution and thank him for providing us with experimental data.

## References

[1] K. Nitsche, J. Straub, The critical hump of Cv under microgravity, results from D-1 spacelab experiment 'Wärmekapazität', Proceeding of the 6th European Symp. on Material Sci. under Microgravity Conditions, ESA SP-256, (1987) 109-116.

[2] A. Onuki, H. Hao H, R.A. Ferrell, Fast adiabatic equilibration in a single-component fluid near the liquid vapor critical point, Phys. Rev. A **41** (1990) 2256-2257.

[3] H. Boukari, J.N. Shaumeyer, M.E. Briggs , R.W. Gammon, Critical speeding up in pure fluids, Phys. Rev. A **41(4)** (1990) 2260-2263.

[4] Y. Garrabos, A. Dejoan, C. Lecoutre, D. Beysens, V. Nikolayev, R. Wunenburger, Piston effect in a supercritical fluid sample cell : A phenomenological approach of the mechanisms, J. Phys. IV France 11 (2001) Pr6-23-Pr6-34.

[5] A.B. Kogan, H. Meyer, Heat transfer and convective onset in a compressible fluid: $^3He$ near the critical point, Phys. rev. E **63**, (2001) 056310-15.

[6] A. Furukawa, H. Meyer, A. Onuki, A.B. Kogan, Convection in a very compressible fluid: Comparison of simulations with experiments, Phys. rev. E **68**, (2003) 056309-7.

[7] P. Carlès, The onset of free convection near the liquidŰvapour critical point.: Part II: Unsteady heating, Physica D: Nonlinear Phenomena, **147**, Issue 1-2, (2000) 36Ű58.

[8] L. El Khouri, P. Carlès, Transition convective dans les fluides supercritiques, 16ème congrès de mécanique, Nice (2003).

[9] S. Amiroudine, Bontoux P., Larroudé P., Gilly B., Direct numerical simulation of instabilities in a two-dimensional near-critical fluid layer heated from below, J. Fluid Mech, **442**, (2001) 119-140.

[10] G. Accary, I. Raspo, B. Bontoux, B. Zappoli, An adaptation of the low Mach number approximation for supercritical fluid buoyant flows, C.R. Mecanique, **333**, (2005) 397-404.

[11] D. Daube, M. Bouafia, R. Bonnefoi, P. Carlès, Déclenchement de la convection Rayleigh Bénard dans l'$He^3$ au voisinage du point critique, 19ème Congrès Français de Mécanique, Marseille (2009).

[12] H. Meyer, A. Kogan, "Onset of convection in a very compressible fluids: the transient toward steady state", Phys. Rev. E **66**, (2002) 056310.

[13] A. Furukawa, A. Onuki, Convective heat transport in compressible fluids, Phys. Rev. E **66**, (2002) 016302-14.

[14] P. Carlès & B. Ugurtas, "The onset of free convection near the liquid-vapour critical point- part I: Stationary initial state", Physica D **126**, (1999) 69-82.

[15] J. Rudnick, M. Barmatz, F. Zhong, Test of a new field-theoretical crossover equation of state, Physica B, Condensed matter, **329-333**, Part 1, (2003) 110-111.

[16] J.M. Hyman, M. Shashkov, Natural discretization for the divergence, gradient and curl on logically rectangular grids, Comput. Maths Appl., **33(4)**, (1997) 81-104.

[17] K. Goda, A multistep technique with implicit difference schemes for calculating two or three dimensional cavity flows, J. Comput. Phys.**30**, (1979) 76-95.

[18] P. Le Quére, R. Masson, P. Perrot, A Chebyshev collocation algorithm for 2D non-Boussinesq convection, J. Comput. Phys. **103**, (1992) 320-335.

[19] J.L. Guermond, P. Minev, Jie Shen, An overview of projection methods for incompressible flows, Comput. Methods Appl. Mech. Engrg **195** (2006) 6011-6045.

[20] M. Akiyama, G.J. Hwang, K.C. Cheng, Experiments on the onset of longitudinal vortices in laminar forced convection between horizontal plates, J. Heat Trans. **93(4)**, (1971) 335-341.

[21] S. Amiroudine, B. Zappoli, Piston-effect-induced thermal oscillations at the Rayleigh Benard threshold in supercritical $^3He$. Phys. Rev. lett. **90(10)**, (2003) 105303.

**List of Figures**